Quantifying the causal effect of cloud controlling factors on marine stratocumulus clouds

Lisa Bock[1], Axel Lauer[1], and Jakob Runge[2, 3, 4]

[1]Deutsches Zentrum für Luft- und Raumfahrt (DLR), Institut für Physik der Atmosphäre, Oberpfaffenhofen, Germany
[2]Deutsches Zentrum für Luft- und Raumfahrt (DLR), Institut für Datenwissenschaften, Jena, Germany
[3]Technische Universität Berlin, Institute of Computer Engineering and Microelectronics, Berlin, Germany
[4]University of Potsdam, Department of Computer Science, Potsdam, Germany

Correspondence: Lisa Bock (lisa.bock@dlr.de)

Abstract. Our incomplete understanding of clouds and their role in cloud-climate feedbacks leads to large uncertainties in climate projections. Using causal inference as an unsupervised machine learning method, we aim at systematically analysing and quantifying causal interdependencies and links between cloud properties and selected cloud-controlling factors. This can be seen as a first step to better understand how these clouds react to changes in controlling factors as a consequence of climate change and to investigate to which degree cloud-climate feedbacks simulated by global climate models are realistic. Here, we focus on marine stratocumulus (Sc) clouds off the coast of South America.

Our results are qualitatively consistent with the findings of previous studies on marine Sc clouds. In contrast to these studies we are also able to quantify the causal effects, revealing that sea surface temperature, lower tropospheric stability, surface sensible heat flux, and 10-m wind speed are the main drivers influencing the properties of marine Sc clouds. While the causal links between these factors and the cloud properties total cloud cover, total cloud water path, and cloud optical depth show similar behaviour, the cloud effective radius remains largely unexplained, suggesting that the background aerosol might play an important role. In contrast, the cloud top pressure is influenced by all cloud-controlling factors investigated, except the surface sensible heat flux. Our findings help to quantify the complex relationships between the properties of marine Sc clouds and relevant cloud-controlling factors.

1 Introduction

As a key component of the hydrological cycle and the Earth's radiation budget, clouds play an important role in both weather and climate. Our incomplete understanding of clouds and their role in cloud-climate feedbacks leads to large uncertainties in climate projections. To improve the representation of clouds in climate models, it is necessary to investigate and quantify the processes that control clouds and their micro- and macrophysical properties. One approach is to quantify the influence of cloud-controlling factors on these properties. As a first step, we focus on one region, the eastern Pacific Ocean west of South America, where mainly one cloud type is present, marine Sc clouds. The processes controlling marine stratocumulus clouds are already well investigated, which allows a consistency check of the results obtained by applying an unsupervised machine learning method in this study.

Marine Sc clouds cover vast areas of the cooler regions of subtropical and mid-latitude oceans on the western side of the continents, where their coverage can exceed 50% annually (Wood, 2012). These low-level clouds reflect incoming solar radiation, leading to a net cooling effect and contributing significantly to the radiation budget. These clouds form when warm, moist air meets cold ocean surfaces, in the boundary layer, often capped by a temperature inversion stabilising the atmosphere. At night, the cloud tops radiate heat into space, a cooling effect triggering vertical, turbulent mixing within the cloud and helping keep them low and widespread. During the day, the sunlight weakens the inversion, reducing turbulence and leading to cloud dissipation. The evolution of marine Sc clouds is driven by atmospheric dynamics, radiation, and oceanic processes, with sunlight and large-scale atmospheric processes influencing their life-time. Changes in their coverage or thickness can significantly impact Earth's energy balance, but their reaction to a warming climate remains uncertain.

Cloud controlling factors (CCFs) influence the formation, growth, and life-time of clouds (Stevens and Brenguier, 2009). Key factors include temperature and humidity, which determine cloud formation once saturation is reached. Vertical air motion, such as updrafts and subsidence, affects cloud formation and growth, with convective motion leading to cumulus type clouds, and descending air leading to dissipating clouds. Wind patterns also play a role, with strong winds shearing clouds and weak winds allowing them to form. Atmospheric stability influences cloud formation, with unstable conditions favouring cumulus and cumulonimbus clouds and stable stratification leading to stratocumulus and altocumulus clouds. Other factors include the large-scale circulation, such as low- and high-pressure systems, radiation, topography, oceanic and land surface conditions, and pollution/aerosols.

Using causal inference (Runge et al., 2023a) as an unsupervised machine learning method we aim to systematically analyse and quantify causal interdependencies and links between cloud properties and their CCFs by causal effect estimation. Causal discovery aims to find and quantify causal interdependencies and dynamical links inside a system such as the Earth's climate (Runge et al., 2019). This approach goes beyond correlation-based measures by systematically excluding common drivers and indirect links.

This study employs causal inference to examine the links between cloud properties and CCFs, which impact cloud formation and their temporal evolution. Causal graphs are estimated from time series data of cloud properties and CCFs from satellite and reanalysis datasets, averaged over selected geographical regions and cloud regimes. Causal effect estimation is used to quantify the strength of individual links in the resulting causal graphs. Section 2 details the satellite and reanalysis data used. Section 3 introduces the "causal inference" method in more detail. Section 4 presents the results. A summary, a discussion of the choice of free parameters for the causal discovery algorithm and an outlook are part of Section 5.

2 Data

In our study, we focus on the following CCFs: sea surface temperature (SST), vertical velocity at 700 hPa, lower tropospheric stability (LTS), sea level pressure, water vapour path, sensible heat flux at the surface, 10-m wind speed. The LTS is calculated by subtracting the potential temperature (θ) at 1000 hPa from the one at 700 hPa: $LTS = \theta_{700\text{hPa}} - \theta_{1000\text{hPa}}$. CCFs are obtained from daily values from satellite datasets provided by ESA CCI (Plummer et al., 2017) and the ERA5 reanalysis (Copernicus

Table 1. Datasets and variables used.

	Variable	Dataset
Cloud properties	Total cloud fraction (clt), Total cloud water path (clwvi), Cloud optical depth (cod), Cloud effective radius (reff), Cloud top pressure (ctp)	ESA CCI Cloud
Cloud-controlling factors	Sea surface temperature (tos)	ESA CCI SST
	Water vapour path (prw)	ESA CCI Watervapour
	Vertical velocity at 700 hPa (wap700), Lower tropospheric stability (LTS), Sea-level pressure (psl), Sensible heat flux at the surface (hfss), 10-m horizontal wind speed (sfcWind)	ERA5

Climate Change Service), see Table 1 and subsections below for details. As cloud properties, we consider total cloud cover, total cloud water path (liquid + ice), cloud optical depth, cloud effective radius, and cloud top pressure, which are all taken from the ESA CCI Cloud (Stengel et al., 2020) dataset (see below).

We use five years of daily data from 2003 to 2007. The data were reformatted to a common format for use with ESMValTool (Eyring et al., 2020; Righi et al., 2020; Lauer et al., 2020; Weigel et al., 2021), which provides downloading and reformatting scripts (so-called "CMORizers") for all data analysed in this study.

2.1 ESA CCI datasets

For this study, we use three datasets from the European Space Agency's Climate Change Initiative (ESA CCI; e.g., Hollmann et al., 2013) which are described below.

2.1.1 ESA CCI Cloud

The version 3 cloud datasets of ESA CCI CLOUD used in this study are based on data retrieved from Advanced Very High Resolution Radiometer (AVHRR) afternoon measurements (post meridiem – PM) aboard satellites of the National Oceanic and Atmospheric Administration (NOAA) Polar Operational Environmental Satellite (POES) missions (Stengel et al., 2020). The datasets contain a comprehensive set of cloud properties and radiative fluxes on a global grid covering the time period 1982 through 2016. Level 3U data (daily instantaneous data) from the ascending orbit are coarse-grained to a horizontal resolution of 0.5° x 0.5°. Variables used are total cloud fraction (clt), total cloud water path (liquid + ice, clwvi), cloud optical thickness (cod), cloud particle effective radius (reff) and cloud-top pressure (ctp). The retrievals provide cloud-top pressure, cloud particle effective radius and cloud optical thickness using measurements at visible, near-infrared and thermal infrared wavelengths. The total cloud water path is calculated from cloud particle effective radius and cloud optical thickness.

2.1.2 ESA CCI SST

This ESA CCI dataset version 3.0 provides global sea surface temperature (SST) data in the period 1980 through 2021 derived from three series of thermal infra-red sensors: the Advanced Very High Resolution Radiometers (AVHRRs), the Along-Track Scanning Radiometers (ATSRs), and the Sea and Land Surface Temperature Radiometers (SLSTRs); and two microwave sensors: the Advanced Microwave Scanning Radiometers (AMSR) (Embury et al., 2024). We use the Level 4 SST CCI analysis product which combines observations from all sensors to produce a global, gridded, gap-free estimate of daily mean SST (Good and Embury).

2.1.3 ESA CCI Watervapour

In the ESA CCI Watervapour project the dataset CM SAF/CCI TCWV-global (COMBI) (Schröder et al.) was created. It combines microwave and near-infrared imager-based TCWV values over the ice-free ocean as well as over land, coastal ocean, and sea ice. For this study, we use the water vapour path of the version 3.1 dataset with a spatial resolution of 0.5°x0.5° and a daily temporal resolution (daily means).

2.2 ERA5

The European Centre for Medium-Range Weather Forecasts (ECMWF) fifth-generation reanalysis ERA5 is based on four-dimensional variational (4D-Var) data assimilation and uses Cycle 41r2 of the Integrated Forecasting System (IFS) (Dee et al., 2011). In this study, ERA5 data obtained from the Copernicus Climate Change Service Climate Data Store (CDS) (Copernicus Climate Change Service) are used. The ERA5 dataset used here has a horizontal resolution of 0.25°x0.25° grid. For more details on the ERA5 dataset, we refer to (Hersbach et al., 2020). Here, we use daily means calculated from hourly data of the variables vertical velocity at 700 hPa (wap700), sea-level pressure (psl), sensible heat flux at the surface (hfss) and 10-m horizontal wind speed (sfcWind) and the lower tropospheric stability derived from the potential temperature (see above).

2.3 Preprocessing of data

We focus in this analysis on the marine Sc region over the Southeast Pacific, which is defined as all ocean grid cells in the geographical region 75°- 95°W, 10°- 30°S (Figure 1). The region is divided into 5°× 5° grid boxes. Within each of these boxes, clouds can be assumed to be in equilibrium with their large-scale environment at this horizontal scale (Klein et al., 1995). As a basis for the PCMCI framework applied here (see Section 3), we pool the time series of all 16 5°× 5° grid box averages over the Southeast Pacific west of South America (Figure 1). The PCMCI algorithm then calculates the causal links with the information from all 16 grid boxes.

To remove the annual cycle as an obvious confounder in the PCMCI causal discovery analysis, anomalized time series are needed. Therefore, we calculate a smoothed annual cycle from the mean daily data averaged over all 5 years and subtract it from the original data. Afterwards, the data are detrended. This results in 12 individual time series per 5°×5° box, 5 of the

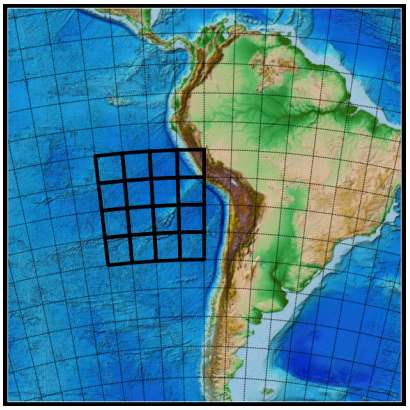

Figure 1. Marine stratocumulus region over the Southeast Pacific analysed in this study divided into 16 5°x5° boxes (75°- 95°W, 10°- 30°S)

different cloud properties and 7 of the individual cloud controlling factors (Figure 2). All time slices of the data where missing values occur in any variable are dismissed while consistently handling time lags.

3 Method

For all causal inference analyses in this study (Runge et al., 2023a), the Python module TIGRAMITE (https://github.com/jakobrunge/tigramite) is used. TIGRAMITE features a number of constraint-based causal discovery methods from the PCMCI framework to reconstruct causal time series graphs from discrete or continuously-valued time series through conditional independence testing. Different algorithm variants and accompanying conditional independence tests allow to adapt the method to different choices of assumptions. The quantification of (total, conditional, and mediated) causal effects based on the estimated causal graphs is also integrated in TIGRAMITE.

3.1 Causal discovery

Here, we apply the causal discovery method LPCMCI (Gerhardus and Runge, 2020), which can learn time series graphs (up to the Markov equivalence class) under the standard assumptions of the Faithfulness and the Markov condition (Gerhardus and Runge, 2020) in addition to causal stationarity. Specifically, LPCMCI can also detect the effect of unobserved confounders, which cannot easily be ruled out in our case. LPCMCI iteratively applies conditional independence testing and logical orientation rules. Like PCMCI+ (Runge, 2020), it first learns lagged parents in order to improve recall and achieve well-calibrated conditional independence tests; for more details, see Gerhardus and Runge (2020). LPCMCI seeks to learn a time series directed partial ancestral graph, which captures the causal time-lagged as well as contemporaneous relationships among the observed variables and can contain directed ($\rightarrow$) and bidirected ($\leftrightarrow$) edges, as well as (partially) unoriented edges $\circ\!\!\rightarrow$ and/or $\circ\!\!-\!\!\circ$. Bidirected arrows imply the presence of unobserved confounding, while directed edges imply causal links (potentially mediated via unobserved variables, and potentially with additional unobserved confounding). We apply robust partial corre-

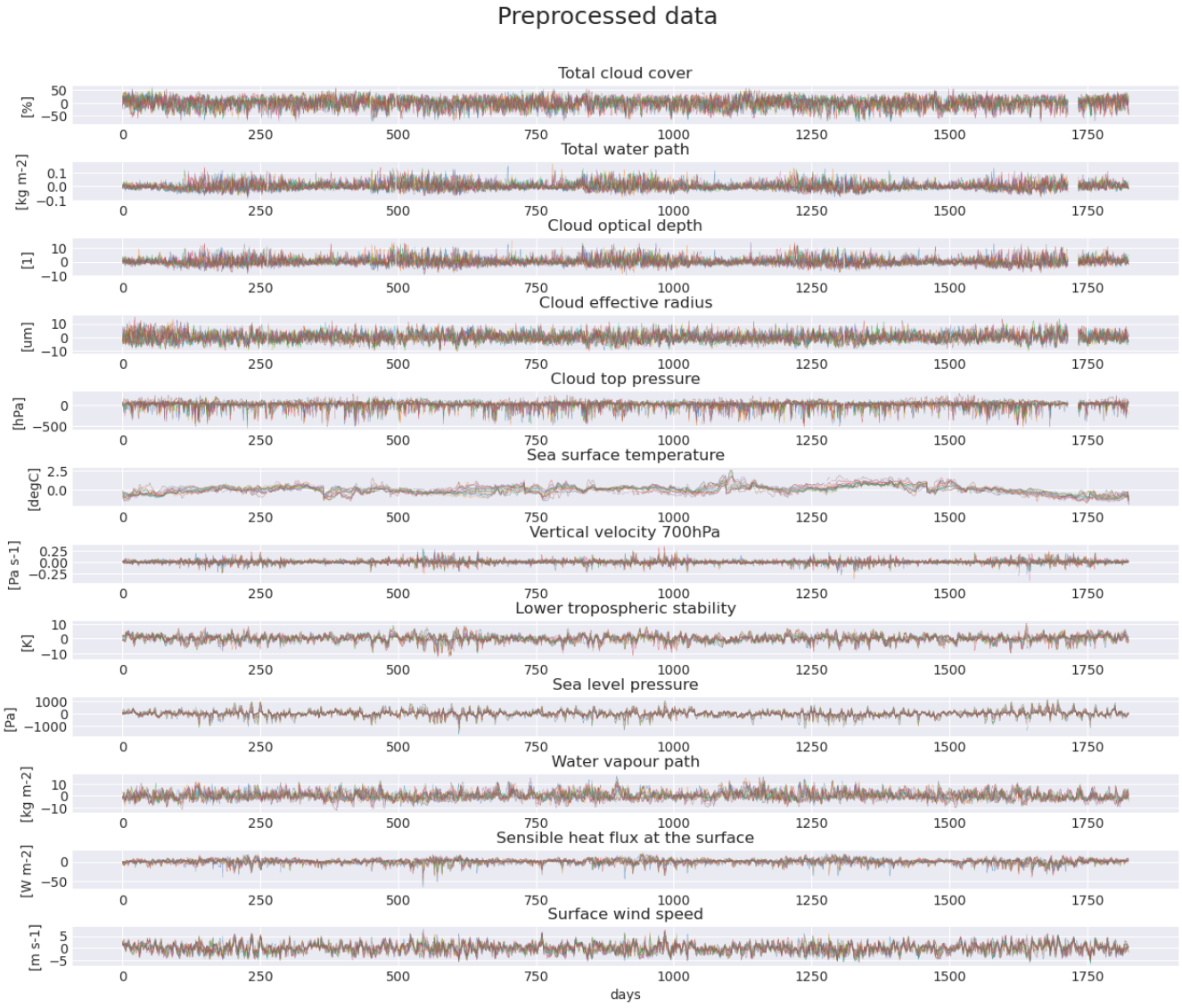

Figure 2. Time series of the 12 deseasonalized and anomalized variables averaged over the 5°× 5° boxes (see Figure 1). The x-axis gives the days since 1 January 2003. From top to bottom: clt (%), clwvi (kg m^{-2}), cod (1), reff (μm), ctp (hPa), tos (°C), wap700 (Pa s^{-1}), lts (K), slp (Pa), prw (kg m^{-2}), hfss (W m^{-2}), and sfcWind (m s^{-1}) (see 1 for variable definitions).

lation (*RobustParCorr*) as a conditional independence test, which is valid for variables related with linear dependencies, but with potentially non-Gaussian noise distributions. RobustParCorr transforms the data to a normal distribution before a standard partial correlation test. The partial correlation is then estimated with ordinary least squares (OLS) regression, and a test for non-zero linear Pearson correlation on the residuals.

To improve the statistical robustness, we combine LPCMCI with a bootstrap aggregation (Debeire et al., 2024) (also implemented in TIGRAMITE). The bootstrap approach is designed for time series causal discovery and preserves the temporal dependencies and time lag structure. Furthermore, next to allowing for a quantification of edge confidence, an aggregation (bagging) of the bootstrapped graphs by majority voting is given, which improves their precision. A value of *boot_samples* = 100 is chosen for this study.

As free parameters of LPCMCI we used: (1) *pc_alpha* = 0.05 defines the significance level of the conditional independence tests, (2) *tau_max* = 1 indicates the maximum considered time lag for the causal time series graph of one day, and (3) *n_preliminary_iterations* = 3 determines the number of causal discovery iterations in LPCMCI (the more, the better, but we chose 3 for computational efficiency). See Section **??** for a discussion of the choice of these free parameters. Additionally, knowledge about existing or non-existing links can be specified via the definition of *link_assumptions*, but was not used in this study.

3.2 Causal effect estimation

Based on the estimated causal graph, we further employ causal effect mediation to quantify the strength of causal links. To this end, we use the path method (**?**Runge et al., 2015), which requires knowledge of a directed time series graph without bidirected or unoriented edges. While LPCMCI allows to detect bidirected edges, the resulting graphs did not contain any of these. Furthermore, in our case all links got oriented. Assuming that the resulting directed links are not confounded, we can then use the path method on the resulting causal graphs. In the path method all dependencies are assumed to be linear and the directed causal effect (path coefficient) of each link is estimated by regressing each variable on its parents. Total and mediated causal effects of a node $X_{t-\tau}$ on a node Y_t, potentially mediated through $M_{t-\tau'}$ can then be estimated as the sum over the products of path coefficient along all causal paths from $X_{t-\tau}$ to Y_t, potentially restricted to only those causal paths that pass through $M_{t-\tau'}$. Confidence intervals were estimated via a bootstrap procedure.

4 Results

Applying LPCMCI, including the extension of the bootstrapping aggregation (Section 3.1) and the linear mediation model to quantify the direct causal effects (Section 3.2) results in a rather convoluted graph (Figure 3). It shows all existing links in the complex system of cloud controlling factors and cloud properties. For further analysis, we extract links showing the effect of cloud controlling factors on cloud properties from this graph. The total (direct + mediated) effect is displayed in Figure 4, which shows the link strengths as absolute changes in the expected value of the cloud property caused by a perturbation of the cloud controlling factor by one standard deviation. The effects are shown for the contemporaneous lag and the lag of one day. The amplitudes or the standard deviations of each variable are shown in Table 2.

The results show a strong negative correlation between sea surface temperature and cloud cover, cloud total water path, and cloud optical depth, which is consistent with previous research (e.g., Klein et al., 2018; Naud et al., 2023; Wood, 2012). This negative correlation can be attributed to the upward expansion and warming of the boundary layer that occurs as sea surface

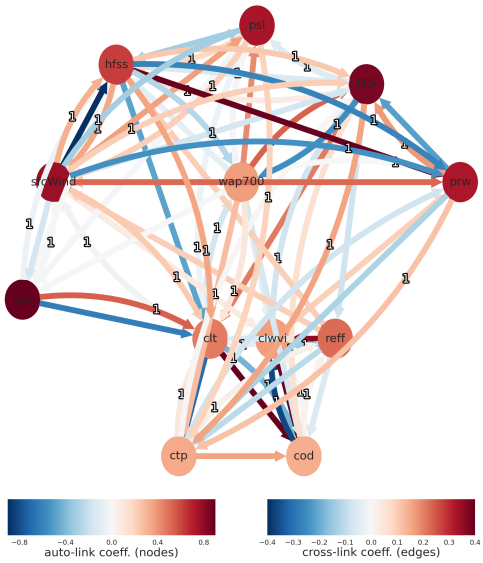

Figure 3. Full causal graph including estimated link strengths showing all links found between all cloud controlling factors and cloud properties.

Table 2. Mean values and standard deviation (STD) of all variables.

Variable	Mean	STD
total cloud fraction	66.59 %	20.17 %
total water path	60.27 g m^{-2}	25.82 g m^{-2}
cloud optical depth	6.09	2.51
cloud effective radius	14.44 μm	3.09 μm
cloud top pressure	862.43 hPa	77.80 hPa
sea surface temperature	293.60 K	0.52 K
vertical velocity at 700 hPa	0.046 Pa s^{-1}	0.039 Pa s^{-1}
lower tropospheric stability	21.55 K	2.13 K
sea level pressure	1017.54 hPa	2.06 hPa
water vapour path	20.39 kg m^{-2}	3.15 kg m^{-2}
sensible heat flux at surface	-11.79 W m^{-2}	5.60 W m^{-2}
surface wind speed	6.93 m s^{-1}	1.80 m s^{-1}

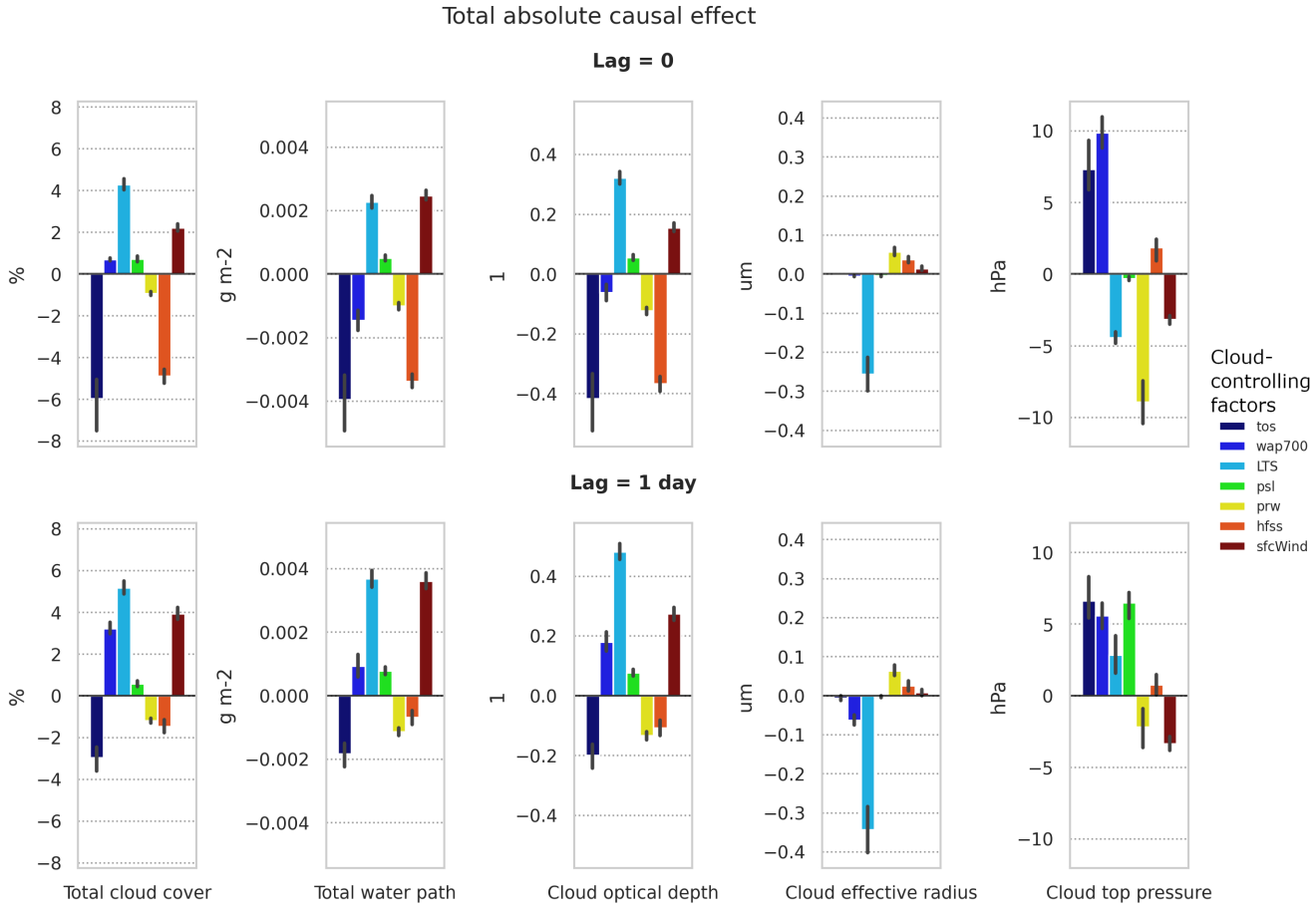

Figure 4. Total (direct + mediated) causal effect of cloud controlling factors on cloud properties for each cloud property. From left to right: clt (%), clwvi (g m^{-2}), cod (1), reff (μm), and ctp (hPa). The top row shows the results for the contemporaneous lag, the bottom row for the lag of one day.

temperature rises (Klein et al., 2018). This, in turn, inhibits cloud formation and reduces persistence, leading to a significant decrease in cloud fraction. Specifically, our analysis reveals that a one-standard-deviation increase in sea surface temperature (approximately 0.5 K; see Table 2) results in an absolute decrease in cloud fraction of 6% on the same day and 3% one day later, as illustrated in Figure 4. In contrast to total cloud water path and cloud optical depth, cloud top pressure exhibits a slight increase with increasing SST.

A positive correlation is found between the vertical velocity at 700 hPa and total cloud fraction, consistent with established knowledge. In environments characterized by strong subsidence, cloud fraction tends to be high because of a strong inversion layer, which stabilizes the cloud layer (Klein et al., 2018). This relationship is more pronounced after a one-day lag, when an increase in subsidence (measured by the vertical velocity at 700 hPa) by one standard deviation (approximately 0.039 Pa s^{-1})

leads to an absolute increase in total cloud fraction of more than 3%. As an additional effect, the cloud top pressure rises by 10 hPa on the same day and by 5 hPa one day later. However, the impact of changes in the subsidence on total water path and cloud optical depth is complex. On the same day, increased subsidence leads to a reduction in both parameters, as the air is more strongly warmed and dried. In contrast, after a one-day lag, the strengthening of the inversion layer associated with subsidence results in an increase in cloud water content and, consequently, cloud optical depth. This suggests a nuanced role of the strength of the subsidence in modulating cloud properties, with both, fast (immediate) and slow (delayed) effects on cloud properties.

The lower tropospheric stability also exerts a profound influence on all cloud properties (Figure 4). It is well established that an increase in lower tropospheric stability, which is typically related to a stronger inversion, effectively traps moisture within the marine boundary layer by reducing mixing, thereby leading to an increase in cloud cover (Klein et al., 2018). Our analysis reveals that this effect of an in increase in LTS is also pronounced on total cloud water path and cloud optical depth. The impact is slightly more pronounced when allowing for a one-day lag, when an increase in lower tropospheric stability of approximately 2 K results in absolute increases of cloud fraction by about 5%, total water path by nearly 0.004 g m^{-2}, and cloud optical depth by almost 0.5. Furthermore, the lower tropospheric stability exhibits the most significant effect on the cloud effective radius, with an increase in LTS of one standard deviation leading to a decrease of 0.25 and 0.35 μm on the same day and after a one-day lag, respectively. In summary, lower tropospheric stability plays a crucial role in modulating Sc cloud properties.

Sea-level pressure only shows a weak positive link to total cloud cover, the total water path and the cloud optical depth. However, its impact on cloud top pressure is more notable, particularly after a one-day lag. Specifically, an increase in sea-level pressure of approximately 2 hPa leads to a corresponding increase in cloud top pressure of around 6 hPa. This suggests that changes in sea-level pressure have a delayed effect on the vertical structure of clouds, with higher sea-level pressure resulting in lower cloud tops ($\sim$50 m).

Water vapour path has only small effects on cloud cover, cloud water path and cloud optical depth, which are found to be slightly negative. Only for the cloud top pressure, we find a strong influence. Specifically, an increase in average atmospheric humidity leads to a significant rise in cloud top heights, indicating that more humid conditions favour higher boundary layer clouds.

The sensible heat flux at the surface describes the transfer of heat between the Earth's surface and the atmosphere driven by turbulent air motion excluding heat transfer resulting from phase changes or water such as condensation or evaporation (Naud et al., 2023). Figure 4 shows a strong negative total causal effect of hfss on cloud cover, cloud water path, and cloud optical depth on the same day. This is expected because a positive sensible heat flux (warming) leads to a more unstable atmosphere, promoting cloud formation and growth. An increase in the sensible heat flux by 5.6 W m^{-2} results in an absolute decrease of 5% in cloud cover, a decrease of 0.003 g m^{-2} in cloud water path, and an almost 0.4 unit decrease in optical depth. The effects on other cloud properties and the lagged impact after one day are significantly smaller.

The positive causal link between surface wind speed and cloud occurrence is most pronounced at a lag of one day. Increased surface wind speed enhances surface-driven shear mixing, which in turn increases the latent heat flux and promotes cloud

formation (Naud et al., 2023). An increase in surface wind speed by one standard deviation (i.e. 1.8 m s^{-1}) results in a 4% increase in cloud cover, an increase of nearly 0.004 g m^{-2} in cloud water path, and an approximately 0.3 unit increase in cloud optical depth. This is accompanied by a decrease of 4 hPa in cloud top pressure, which corresponds to higher cloud tops by about 30 m.

The most important causal effects on cloud properties are related to sea surface temperature, lower tropospheric stability, sensible heat flux at the surface and surface wind speed. From all cloud-controlling factors considered in this study, only lower tropospheric stability has a significant causal effect on the cloud effective radius. For the cloud top pressure also the vertical velocity at 700 hPa has a strong influence.

5 Discussions and Conclusions

To gain a deeper understanding of the underlying mechanisms determining observed properties of marine Sc clouds, we applied causal inference techniques to discover causal relationships and subsequently quantified their effects.

The links found between cloud-controlling factors and cloud properties are in agreement with previous studies on marine Sc clouds, lending credibility to our findings. In addition, we were able to quantify the causal effects on all five considered cloud properties. Specifically, our analysis revealed that the main influences on cloud properties are exerted by changes in sea surface temperature, lower tropospheric stability, sensible heat flux at the surface, and near-surface wind speed. In detail, the strength of the causal links to the three cloud properties, total cloud cover, total cloud water path and cloud optical depth, is of a similar relative magnitude for each of these three cloud-controlling factors with small variations. There is a strong negative link on the same day with sea surface temperature with a decrease of about 6% in cloud fraction, about 0.004 g m-2 in total water path and about 0.4 in optical depth by an increase of approximately 0.5 K. The links with a time lag of one day are about half as strong. Also, there is a strong negative link originated by the surface heat flux with a decrease on the same day of about 5% in cloud fraction, 0.003 g m^{-2} in total water path and 0.4 in optical depth by an increase of approximately 5.6 W m^{-2}. With a time lag of one day, however, these negative links are much smaller. In contrast, there is a strong positive link from lower tropospheric stability and near-surface wind speed with these three cloud properties for both lags. An increase of lower tropospheric stability by about 2 K leads after one day to an increase of about 5% in cloud fraction, 0.004 g m^{-2} in total water path and 0.5 in optical depth. The causal links for the same day are slightly less strong. Similarly, for near-surface wind-speed, the links are stronger with a lag of one day than on the same day. An increase of near-surface wind speed of about 1.8 m s^{-1} leads to an increase of about 4% in cloud fraction, about 0.004 g m^{-2} in total water path and about 0.3 in optical depth. On the same day, the links are about half as strong. In contrast, cloud effective radius is only slightly affected by the lower tropospheric stability, an increase of LTS by 2 K leads to a decrease in effective radius of about 0.25 and 0.35μm on the same day and with a lag of one day, respectively. This means that effects on cloud effective radius remain largely unexplained by the cloud-controlling factors considered in this study. This suggests that the inclusion of other cloud-controlling factors such as e.g. the properties of the background aerosol might be necessary to also account for relevant aerosol-cloud interactions. Cloud top pressure is also only

weakly affected by the cloud-controlling factors investigated here. In contrast to effective radius, cloud top pressure is affected by all different cloud-controlling factors apart from sensible heat flux at the surface.

One of the challenges in applying causal discovery is the choice of the free parameters. Specifically, these parameters include the significance level of the conditional independence tests (*pc_alpha*), the maximum considered time lag for the causal graph (*tau_max*), and the number of iterations in the preliminary phase of LPCMCI (*n_preliminary_iterations*). We conducted sensitivity tests to study the effect of varying these parameters.

Our results show that the number of preliminary iterations (*n_preliminary_iterations*) does not significantly impact the causal graph, suggesting that the algorithm is rather robust to the specific setting of this parameter. However, the choice of maximum time lag (*tau_max*) does affect the results significantly. We chose *tau_max* = 1 as marine boundary layer clouds respond rather rapidly to changes in their environment, typically within hours. As the satellite measurements of the cloud properties are taken at the overpass times specific to the satellite, not all parameters are captured at the same time of the day. For this reason we also consider links with a time lag of one day. To test the sensitivity, we varied the hyperparameter *tau_max* in the range of [0, 1, 2]. When using *tau_max* = 0, several links are missing, e.g. no causal influence by the sensible heat flux on the surface on cloud properties is shown. This is expected because these links operate on longer time scales and makes *tau_max* = 0 an inadequate choice. When estimating the causal graph for *tau_max* = 2, we obtain similar link structures as for *tau_max* = 1.

We also investigated the sensitivity of the results to the exact choice of the significance level of the conditional independence tests (*pc_alpha*). Our results show that values of *pc_alpha* in [0.01, 0.05, 0.1] yield consistent results, with smaller significance levels providing fewer links but stronger evidence. Nevertheless, the main causal links remain consistent across different values of *pc_alpha*. Therefore, we select a commonly used significance level of *pc_alpha* = 0.05 for our analysis.

A promising new application of the causal discovery techniques used in this paper is the regime-oriented causal model evaluation. A process-oriented evaluation of climate models can be conducted by comparing the causal graphs derived from e.g. satellite and reanalysis data or very detailed and high-resolution models with those generated from climate models used for climate projections. For this, daily output of cloud properties and cloud-controlling factors from climate models are required to investigate the sensitivities of cloud properties to changes in cloud-controlling factors. It can then be quantitatively assessed whether relevant processes are sufficiently realistic or if important processes are missing. A quantification of the links is particularly relevant for investigating to which degree cloud-climate feedbacks of marine Sc clouds simulated by global climate models are trustworthy.

Application of the causal discovery method to other cloud regimes, however, may pose some challenges. Clouds that are transported significantly by advection related e.g. to the large-scale atmospheric circulation or frontal systems cannot be regarded as stationary. In these cases, it would be necessary to develop a methodology that samples the time series of cloud properties and cloud-controlling factors along the trajectories of the clouds. Application of this method would also become much more complex if not impossible in case of a varying mixture of different cloud types. This applies in particular to coarse-resolution grid boxes of many climate models in which different cloud types are frequently mixed during the course of one day. In this case, a method to distinguish between the different cloud type in a grid box would be needed.

Code and data availability. The code is written in Python and will be available under Zenodo. The ESA CCI Cloud and ESA CCI SST data are freely available at can be obtained from https://public.satproj.klima.dwd.de/data/ESA_Cloud_CCI/CLD_PRODUCTS/v3.0/L3U/ and https://dap.ceda.ac.uk/neodc/eocis/data/global_and_regional/sea_surface_temperature/CDR_v3/Analysis/L4/v3.0.1/, respectively. For the ESA CCI Watervapour data, a registration is needed before the data can be downloaded from https://wui.cmsaf.eu/safira/action/viewDoiDetails?acronym=COMBI_V001. ERA5 data are provided by the ECMWF at https://doi.org/10.24381/cds.adbb2d47, which requires registration. The LPCMCI and the Linear Mediation algorithm, part of the Tigramite package, are available under the following public Zenodo repository: https://doi.org/10.5281/zenodo.7747255 (Runge et al., 2019, 2023b).

Author contributions. LB performed the analysis, prepared all figures, and led the writing of the paper. JR helped with applying the method and writing the paper. AL contributed to the scientific interpretation of the results and the writing of the paper.

Competing interests. The authors declare that they have no conflict of interest.

Acknowledgements. This work was funded by support from the ESA Climate Change Initiative for the Climate Modelling User Group (CMUG) under contract 4000125156/18/I-NB and by the European Research Council (ERC) Synergy Grant "Understanding and Modelling the Earth System with Machine Learning (USMILE)" under the Horizon 2020 research and innovation programme (Grant agreement No. 855187). This work used resources of the Deutsches Klimarechenzentrum (DKRZ) granted by its Scientific Steering Committee (WLA) under project ID bd1083. We thank Kevin Debeire (DLR) for helpful comments on the manuscript.

References

Copernicus Climate Change Service: Complete ERA5 global atmospheric reanalysis, https://doi.org/10.24381/CDS.143582CF.

Debeire, K., Gerhardus, A., Runge, J., and Eyring, V.: Bootstrap aggregation and confidence measures to improve time series causal discovery, in: Proceedings of the Third Conference on Causal Learning and Reasoning, edited by Locatello, F. and Didelez, V., vol. 236 of *Proceedings of Machine Learning Research*, pp. 979–1007, PMLR, https://proceedings.mlr.press/v236/debeire24a.html, 2024.

Dee, D. P., Uppala, S. M., Simmons, A. J., Berrisford, P., Poli, P., Kobayashi, S., Andrae, U., Balmaseda, M. A., Balsamo, G., Bauer, P., Bechtold, P., Beljaars, A. C. M., van de Berg, L., Bidlot, J., Bormann, N., Delsol, C., Dragani, R., Fuentes, M., Geer, A. J., Haimberger, L., Healy, S. B., Hersbach, H., Hólm, E. V., Isaksen, L., Kållberg, P., Köhler, M., Matricardi, M., McNally, A. P., Monge-Sanz, B. M., Morcrette, J.-J., Park, B.-K., Peubey, C., de Rosnay, P., Tavolato, C., Thépaut, J.-N., and Vitart, F.: The ERA–Interim reanalysis: configuration and performance of the data assimilation system, Quarterly Journal of the Royal Meteorological Society, 137, 553–597, https://doi.org/10.1002/qj.828, 2011.

Embury, O., Merchant, C. J., Good, S. A., Rayner, N. A., Høyer, J. L., Atkinson, C., Block, T., Alerskans, E., Pearson, K. J., Worsfold, M., McCarroll, N., and Donlon, C.: Satellite-based time-series of sea-surface temperature since 1980 for climate applications, Scientific data, 11, 326, https://doi.org/10.1038/s41597-024-03147-w, 2024.

Eyring, V., Bock, L., Lauer, A., Righi, M., Schlund, M., Andela, B., Arnone, E., Bellprat, O., Brötz, B., Caron, L.-P., Carvalhais, N., Cionni, I., Cortesi, N., Crezee, B., Davin, E. L., Davini, P., Debeire, K., de Mora, L., Deser, C., Docquier, D., Earnshaw, P., Ehbrecht, C., Gier, B. K., Gonzalez-Reviriego, N., Goodman, P., Hagemann, S., Hardiman, S., Hassler, B., Hunter, A., Kadow, C., Kindermann, S., Koirala, S., Koldunov, N., Lejeune, Q., Lembo, V., Lovato, T., Lucarini, V., Massonnet, F., Müller, B., Pandde, A., Pérez-Zanón, N., Phillips, A., Predoi, V., Russell, J., Sellar, A., Serva, F., Stacke, T., Swaminathan, R., Torralba, V., Vegas-Regidor, J., von Hardenberg, J., Weigel, K., and Zimmermann, K.: Earth System Model Evaluation Tool (ESMValTool) v2.0 – an extended set of large-scale diagnostics for quasi-operational and comprehensive evaluation of Earth system models in CMIP, Geoscientific Model Development, 13, 3383–3438, https://doi.org/10.5194/gmd-13-3383-2020, 2020.

Gerhardus, A. and Runge, J.: High-recall causal discovery for autocorrelated time series with latent confounders, Advances in Neural Information Processing Systems, 2020.

Good, S. A. and Embury, O.: ESA Sea Surface Temperature Climate Change Initiative (SST_cci): Level 4 Analysis product, version 3.0, https://doi.org/10.5285/4A9654136A7148E39B7FEB56F8BB02D2.

Hersbach, H., Bell, B., Berrisford, P., Hirahara, S., Horányi, A., Muñoz-Sabater, J., Nicolas, J., Peubey, C., Radu, R., Schepers, D., Simmons, A., Soci, C., Abdalla, S., Abellan, X., Balsamo, G., Bechtold, P., Biavati, G., Bidlot, J., Bonavita, M., de Chiara, G., Dahlgren, P., Dee, D., Diamantakis, M., Dragani, R., Flemming, J., Forbes, R., Fuentes, M., Geer, A., Haimberger, L., Healy, S., Hogan, R. J., Hólm, E., Janisková, M., Keeley, S., Laloyaux, P., Lopez, P., Lupu, C., Radnoti, G., de Rosnay, P., Rozum, I., Vamborg, F., Villaume, S., and Thépaut, J.-N.: The ERA5 global reanalysis, Quarterly Journal of the Royal Meteorological Society, 146, 1999–2049, https://doi.org/10.1002/qj.3803, 2020.

Hollmann, R., Merchant, C. J., Saunders, R., Downy, C., Buchwitz, M., Cazenave, A., Chuvieco, E., Defourny, P., de Leeuw, G., Forsberg, R., Holzer-Popp, T., Paul, F., Sandven, S., Sathyendranath, S., van Roozendael, M., and Wagner, W.: The ESA Climate Change Initiative: Satellite Data Records for Essential Climate Variables, Bulletin of the American Meteorological Society, 94, 1541–1552, https://doi.org/10.1175/BAMS-D-11-00254.1, 2013.

Klein, S. A., Hartmann, D. L., and Norris, J. R.: On the Relationships among Low-Cloud Structure, Sea Surface Temperature, and Atmospheric Circulation in the Summertime Northeast Pacific, Journal of Climate, 8, 1140–1155, https://doi.org/10.1175/1520-0442(1995)008<1140:OTRALC>2.0.CO;2, 1995.

Klein, S. A., Hall, A., Norris, J. R., and Pincus, R.: Low-Cloud Feedbacks from Cloud-Controlling Factors: A Review, in: Shallow Clouds, Water Vapor, Circulation, and Climate Sensitivity, edited by Pincus, R., Winker, D., Bony, S., and Stevens, B., pp. 135–157, Springer International Publishing, Cham, https://doi.org/10.1007/978-3-319-77273-8_7, 2018.

Lauer, A., Eyring, V., Bellprat, O., Bock, L., Gier, B. K., Hunter, A., Lorenz, R., Pérez-Zanón, N., Righi, M., Schlund, M., Senftleben, D., Weigel, K., and Zechlau, S.: Earth System Model Evaluation Tool (ESMValTool) v2.0 – diagnostics for emergent constraints and future projections from Earth system models in CMIP, Geoscientific Model Development, 13, 4205–4228, https://doi.org/10.5194/gmd-13-4205-2020, 2020.

Naud, C. M., Elsaesser, G. S., and Booth, J. F.: Dominant Cloud Controlling Factors for Low-Level Cloud Fraction: Subtropical Versus Extratropical Oceans, Geophysical Research Letters, 50, e2023GL104 496, https://doi.org/10.1029/2023GL104496, 2023.

Plummer, S., Lecomte, P., and Doherty, M.: The ESA Climate Change Initiative (CCI): A European contribution to the generation of the Global Climate Observing System, Remote Sensing of Environment, 203, 2–8, https://doi.org/10.1016/j.rse.2017.07.014, 2017.

Righi, M., Andela, B., Eyring, V., Lauer, A., Predoi, V., Schlund, M., Vegas-Regidor, J., Bock, L., Brötz, B., de Mora, L., Diblen, F., Dreyer, L., Drost, N., Earnshaw, P., Hassler, B., Koldunov, N., Little, B., Loosveldt Tomas, S., and Zimmermann, K.: Earth System Model Evaluation Tool (ESMValTool) v2.0 – technical overview, Geoscientific Model Development, 13, 1179–1199, https://doi.org/10.5194/gmd-13-1179-2020, 2020.

Runge, J.: Discovering contemporaneous and lagged causal relations in autocorrelated nonlinear time series datasets, in: Proceedings of the 36th Conference on Uncertainty in Artificial Intelligence (UAI), edited by Peters, J. and Sontag, D., vol. 124 of *Proceedings of Machine Learning Research*, pp. 1388–1397, PMLR, https://proceedings.mlr.press/v124/runge20a.html, 2020.

Runge, J., Petoukhov, V., Donges, J. F., Hlinka, J., Jajcay, N., Vejmelka, M., Hartman, D., Marwan, N., Paluš, M., and Kurths, J.: Identifying causal gateways and mediators in complex spatio-temporal systems, Nature communications, 6, 8502, https://doi.org/10.1038/ncomms9502, 2015.

Runge, J., Nowack, P., Kretschmer, M., Flaxman, S., and Sejdinovic, D.: Detecting and quantifying causal associations in large nonlinear time series datasets, Science advances, 5, eaau4996, https://doi.org/10.1126/sciadv.aau4996, 2019.

Runge, J., Gerhardus, A., Varando, G., Eyring, V., and Camps-Valls, G.: Causal inference for time series, Nature Reviews Earth & Environment, 4, 487–505, https://doi.org/10.1038/s43017-023-00431-y, 2023a.

Runge, J., Gillies, E., Strobl, E. V., and Palachy-Affek, S.: jakobrunge/tigramite: Tigramite 5.2, https://doi.org/10.5281/ZENODO.6247836, 2023b.

Schröder, M., Danne, O., Falk, U., Niedorf, A., Preusker, R., Trent, T., Brockmann, C., Fischer, J., Hegglin, M., Hollmann, R., and Pinnock, S.: A combined high resolution global TCWV product from microwave and near infrared imagers - COMBI, https://doi.org/10.5676/EUM_SAF_CM/COMBI/V001.

Stengel, M., Stapelberg, S., Sus, O., Finkensieper, S., Würzler, B., Philipp, D., Hollmann, R., Poulsen, C., Christensen, M., and McGarragh, G.: Cloud_cci Advanced Very High Resolution Radiometer post meridiem (AVHRR-PM) dataset version 3: 35-year climatology of global cloud and radiation properties, Earth System Science Data, 12, 41–60, https://doi.org/10.5194/essd-12-41-2020, 2020.

Stevens, B. and Brenguier, J.-L.: Cloud-controlling Factors: Low Clouds, in: Clouds in the Perturbed Climate System: Their Relationship to Energy Balance, Atmospheric Dynamics, and Precipitation, edited by Heintzenberg, Jost, and Robert J. Charlson, The MIT Press, Cambridge, MA, https://doi.org/10.7551/mitpress/8300.003.0010, 2009.

Weigel, K., Bock, L., Gier, B. K., Lauer, A., Righi, M., Schlund, M., Adeniyi, K., Andela, B., Arnone, E., Berg, P., Caron, L.-P., Cionni, I., Corti, S., Drost, N., Hunter, A., Lledó, L., Mohr, C. W., Paçal, A., Pérez-Zanón, N., Predoi, V., Sandstad, M., Sillmann, J., Sterl, A., Vegas-Regidor, J., von Hardenberg, J., and Eyring, V.: Earth System Model Evaluation Tool (ESMValTool) v2.0 – diagnostics for extreme events, regional and impact evaluation, and analysis of Earth system models in CMIP, Geoscientific Model Development, 14, 3159–3184, https://doi.org/10.5194/gmd-14-3159-2021, 2021.

Wood, R.: Stratocumulus Clouds, Monthly Weather Review, 140, 2373–2423, https://doi.org/10.1175/MWR-D-11-00121.1, 2012.